Quantum Skyrmion Lattices in Heisenberg Ferromagnets

Andreas Haller, Solofo Groenendijk, Alireza Habibi, Andreas Michels, and Thomas L. Schmidt
Department of Physics and Materials Science, University of Luxembourg, L-1511 Luxembourg, Luxembourg
(Dated: December 24, 2021)

Skyrmions are topological magnetic textures which can arise in non-centrosymmetric ferromagnetic materials. In most systems experimentally investigated to date, skyrmions emerge as classical objects. However, the discovery of skyrmions with nanometer length scales has sparked interest in their quantum properties. Quantum corrections to the classical magnetic textures have already been considered in the semiclassical regime. Here, we go beyond this limit by investigating quantum skyrmions in the deep quantum regime. We use density matrix renormalization group techniques to study two-dimensional spin-1/2 Heisenberg ferromagnets with Dzyaloshinskii-Moriya interactions and discover a broad region in the zero temperature phase diagram which hosts quantum skyrmion lattice ground states. We argue that this novel quantum skyrmion phase can be detected experimentally in the magnetization profile via local magnetic polarization measurements as well as in the spin structure factor measurable via neutron scattering experiments. Finally, we explore the resulting quantum skyrmion state, analyze its real space polarization profile and show that it is a non-classical state featuring entanglement between quasiparticle and environment mainly localized near the boundary spins of the skyrmion.

I. INTRODUCTION

Magnetic skyrmions are vortex-like quasiparticles characterized by a nontrivial topological invariant in real space [1–4]. These states are typically found in non-centrosymmetric ferromagnets in a certain range of external magnetic field and temperature, and are stabilized by an antisymmetric spin exchange energy, termed Dzyaloshinskii-Moriya interaction (DMI) [1]. After their first detection in a magnetic system by a neutron diffraction experiment in 2009 [5], and a full microscopic tomography by electron microscopy in 2010 [6], intense follow-up studies revealed intriguing dynamical properties, rendering skyrmions potentially useful for novel memory and computing devices [7–11]. Usually, the skyrmions encountered in these systems arise from thermal fluctuations and extend over length scales that are much larger than the interatomic distance and thus behave as classical objects. However, smaller skyrmions do exist [12] and have already created interest in possible quantum properties of skyrmions. Several works have predicted quantum behavior of skyrmions by using classical magnetic textures as a starting point and studying quantum corrections in the semiclassical regime [13–15].

Beyond this semiclassical limit, some works have indicated that quantum analogs of classical skyrmions might exist in spin systems. The authors of Ref. [16] used a multiscale approach to demonstrate that mesoscopic magnetization vortices are stabilized by quantum fluctuations [17], which suggests the possibility of inherently quantum-mechanical counterparts of these states at zero temperature. So far, attempts to classify skyrmion excitations with sizes comparable to the interatomic spacing have been made in frustrated quantum lattice systems [18] and ferromagnetic lattices with DMI [19, 20]. Several geometries have been studied to understand the quantum analogs of classical skyrmions, and quantitative results have been obtained by numerical diagonalization of the Hamiltonian. Since the dimension of the quantum Hamiltonian scales exponentially with the number of lattice sites, such exact diagonalization (ED) strategies are limited to small system sizes containing at most ≈ 30 spin-1/2 sites (without exploiting symmetries). Although DMI interactions are among the most popular to investigate the formation of classical skyrmion phases, their quantum analogs are analytically hard to handle and quantitative results beyond system sizes amenable for ED are still lacking. As an alternative route to quantum skyrmions which avoids DMI, frustrated spin lattice systems were studied in Ref. [18]. Using ED for small systems and analytical spin wave theory, the authors identified skyrmions with magnon bound states, and developed a phenomenological theory based on a trial wave function. For the latter, however, a product state was assumed, so internal entanglement of quantum skyrmions was neglected.

Here, we use the density matrix renormalization group (DMRG) algorithm to explore ferromagnetic phases of quantum spin-1/2 Heisenberg models with DMI and uniaxial anisotropy. As our main result, we discover a zero temperature quantum phase with a nontrivial magnetic spin texture that signals an emergent quantum skyrmion lattice. This novel phase was previously overlooked because it appears only beyond a critical system size which for realistic parameters is larger than the system sizes amenable to ED. We identify three ferromagnetic phases that can be directly observed and distinguished in the space-resolved magnetization profile. Furthermore, we argue that the polarization gives access to the zero temperature phase diagram of the model under investigation. Contrary to similar quasiparticles found in frustrated lattices [18] or quantum skyrmions embedded in a classical magnet [20], we show that the skyrmion lattice phase reported in this letter emerges from entangled spin-1/2 pairs, which bear witness to a genuine quantum mechanical origin without classical analog.

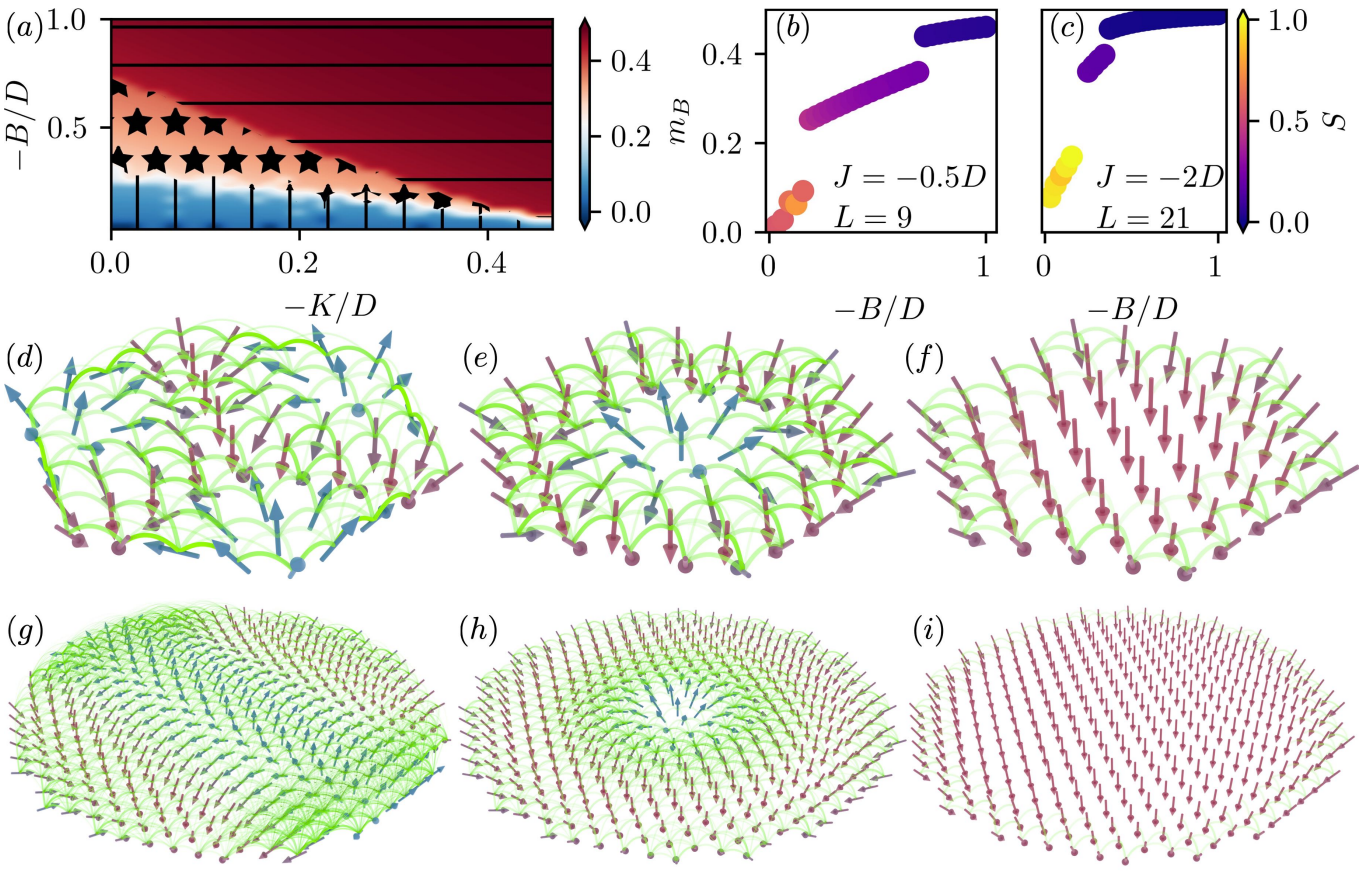

FIG. 1. (a) Zero temperature phase diagram of the quantum spin-1/2 model defined by the Hamiltonian in Eq. (1) and Eq. (2) on a triangular 9×9 lattice, obtained via the average polarization $\bar{m}^z$ (shown in color) as a function of the uniaxial anisotropy K and the external field strength B. The ferromagnetic exchange interaction is fixed to $J = -0.5D$. Hatches highlight the maximum entanglement entropy S: vertical lines signal highly entangled spin waves with $S \geq 0.7$, horizontal lines correspond to field-polarized magnetic states with $S \leq 0.2$ and stars mark entangled quantum skyrmions with values $0.2 < S < 0.7$. In panels (b) and (c), we show $\bar{m}^z$ (vertical axis) and S (color scale) for $K = 0$ for two circular systems with different diameters L and different exchange couplings J. (d)-(i) Representative pictures for the states simulated at the center of the phases in panels (b) and (c): we plot the local polarization as colored arrows and the concurrence by green lines connecting pairs of sites. Representative spin wave states are plotted in panels (d) and (g), quantum skyrmion states in panels (e) and (h), and field-polarized states in panels (f) and (i). The system diameter is $L = 9$ for panels (d)-(f) and $L = 21$ for panels (g)-(i), resulting in 61 and 367 spin-1/2 sites, respectively.

II. RESULTS

Model. We study the zero temperature phase diagram of a quantum spin-1/2 Heisenberg model with DMI and external magnetic field. The Hamiltonian reads:

$$\hat{H} = \sum_{\langle \boldsymbol{r}, \boldsymbol{r}' \rangle} \left[J \hat{\boldsymbol{S}}_{\boldsymbol{r}} \cdot \hat{\boldsymbol{S}}_{\boldsymbol{r}'} + \boldsymbol{D}_{\boldsymbol{r}'-\boldsymbol{r}} \cdot \left(\hat{\boldsymbol{S}}_{\boldsymbol{r}} \times \hat{\boldsymbol{S}}_{\boldsymbol{r}'} \right) \right] + \sum_{\boldsymbol{r}} \boldsymbol{B} \cdot \hat{\boldsymbol{S}}_{\boldsymbol{r}}, \tag{1}$$

where $\hat{\boldsymbol{S}}_{\boldsymbol{r}} = \hbar \hat{\boldsymbol{\sigma}}_{\boldsymbol{r}}/2$, with Pauli matrices $\hat{\sigma}_{\alpha,\boldsymbol{r}}$ for $\alpha \in \{x, y, z\}$, denotes a spin-1/2 operator at position $\boldsymbol{r}$ and $\langle \boldsymbol{r}, \boldsymbol{r}' \rangle$ represents a sum over nearest-neighbor lattice sites. $J < 0$ is the ferromagnetic exchange coupling strength, $\boldsymbol{D}_{\boldsymbol{r}'-\boldsymbol{r}}$ is the DMI vector, and $\boldsymbol{B} = B\hat{\boldsymbol{e}}_z$ denotes the applied magnetic field along the z axis. We furthermore consider perturbations due to an uniaxial magnetic anisotropy with strength K,

$$\hat{H}_K = \sum_{\langle \boldsymbol{r}, \boldsymbol{r}' \rangle} K \hat{S}^z_{\boldsymbol{r}} \hat{S}^z_{\boldsymbol{r}'}. \tag{2}$$

We solve the above Hamiltonian numerically on different two-dimensional Bravais lattices consisting of lattice sites $\boldsymbol{r} = \sum_i n_i \boldsymbol{a}_i$ spanned by basis vectors $\boldsymbol{a}_{1,2}$ with $a_{z,i} = 0$. In this notation, the DMI vectors read

$$\boldsymbol{D}_{\boldsymbol{a}_i} = D\hat{\boldsymbol{e}}_z \times \boldsymbol{a}_i, \tag{3}$$

with the positive DMI vector amplitude $D > 0$.

Note that we apply the external magnetic field $\boldsymbol{B}$ parallel to the lattice plane normal $\hat{\boldsymbol{e}}_z$. Without loss of generality, we assume negative values $B < 0$ such that field-polarized spins are eigenstates of $\hat{S}^z_{\boldsymbol{r}}$ with eigenvalue

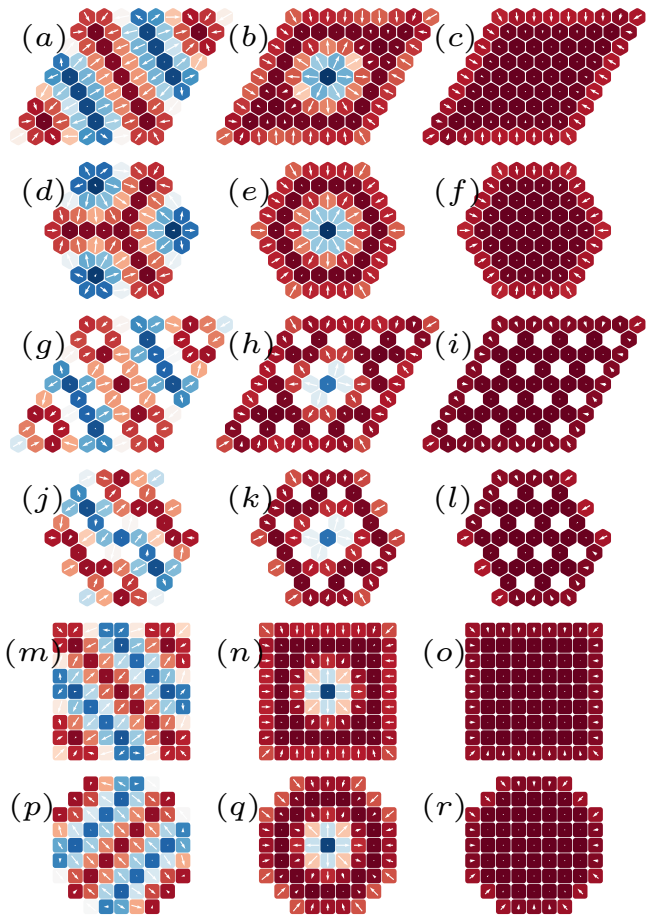

FIG. 2. Local polarization $m_{z,\boldsymbol{r}}$ (in color) of the ground states of the three different phases as obtained by DMRG simulations of Eq. (1). Arrows depict the direction and size of the magnetization components $m_{x/y,\boldsymbol{r}}$ perpendicular to the external field. We study different triangular (a)-(l) and square (m)-(r) systems with regular boundary conditions (odd rows) and circular boundary conditions (even rows). The parameters used are $J = -D/2$ and $K = 0$, with a varying external field $B = -0.1D$ (first column), $B = -0.5D$ (second column) and $B = -1.0D$ (third column). We find quantum skyrmions for system sizes larger than a critical diameter $L \approx 8a$, irrespective of the lattice symmetries and boundary conditions.

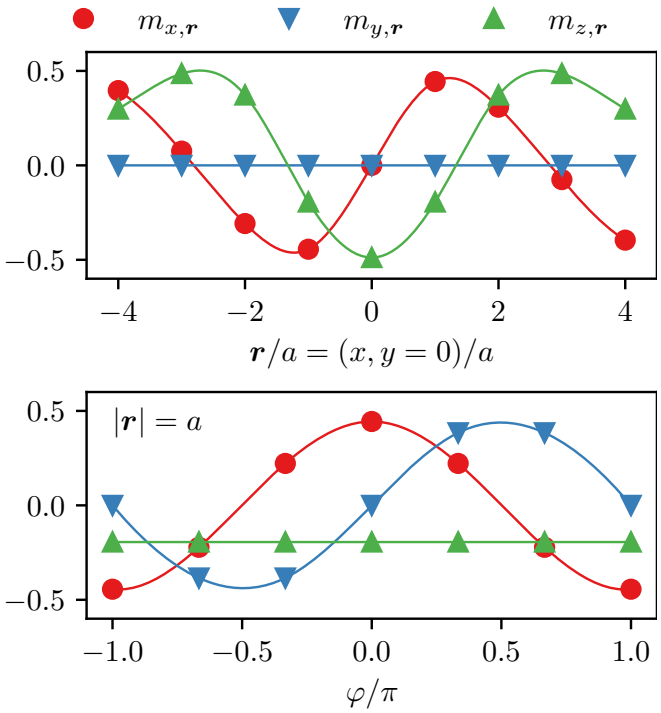

FIG. 3. Components of the local polarization $\boldsymbol{m}_{\boldsymbol{r}}$ of the centered skyrmion ground state depicted in Fig. 2(e). From the radial winding at fixed $y = 0$ (upper panel) the radius of the quasiparticle can be estimated to $r_0 \approx 3a$. The azimuthal projection (lower panel) at fixed $|\boldsymbol{r}| = a$ reveals a sinusoidal winding of the y/x components, with a phase difference of π.

$+1/2$ and therefore align with the plane normal. For convenience, we will express interatomic distances in units of the lattice constants $a_i = |\boldsymbol{a}_i|$ and energies in units of D, with $\hbar = 1$. The Hamiltonian (1) may be seen as the quantum counterpart of typical classical spin models which give rise to magnetic skyrmions [1–4]. In this work, we discuss the emergence of quantum skyrmions and quantum skyrmion lattices in two-dimensional triangular and square lattices at zero temperature and with different boundary conditions (see Fig. 2).

Individual quantum skyrmions. For small system diameters ($L \lessapprox 5a$), the exact eigenvalues and eigenvectors of the full Hamiltonian can be computed numerically, for instance by the Lanczos or Arnoldi algorithms, and we first cross-checked our own exact diagonalization (ED) codes by reproducing the results of Ref. [19]. To ensure the correctness of our findings, we further compared expectation values computed from the matrix product states (MPS) obtained by DMRG with ED results for all system sizes amenable for ED and found quantitative agreement up to a self-imposed accuracy δ (see Section IV). This shows that finite-size ground states of the spin-1/2 Hamiltonian can be approximated faithfully with MPS. In fact, the reliability of DMRG for 2D spin-1/2 quantum Heisenberg models has already been demonstrated in numerous works, with a strong bias towards frustrated antiferromagnets and spin liquids, which are prime examples of the most demanding systems to simulate numerically due to the presence of topological order and long-range entanglement [21–51]. In this work, we focus on the computationally less demanding scenario of magnetically ordered phases hosting skyrmions and field-polarized states.

Beyond a critical system diameter of $L \approx 8a$, we find values of D and B for which the ground state of the Hamiltonian $\hat{H}$ hosts skyrmion-like spin textures confined in the interior (bulk) of the lattice, which we display in Fig. 2. We checked that these skyrmion wave functions correspond to approximate eigenstates of the Hamiltonian by computing the energy variance ε and performed

a linear extrapolation towards results without numerical errors (see Section IV for a discussion).

We compute the components of the spin magnetization, which are local expectation values $\boldsymbol{m_r} = \langle \hat{\boldsymbol{S}}_{\boldsymbol{r}} \rangle$. Since $m_{z,\boldsymbol{r}}$ is parallel to the external field, we call this magnetization component the polarization. For $B \approx J = -D/2$, the local spin profiles yield magnetization textures similar to those obtained for classical skyrmion configurations of the Néel (hedgehog) type: the central spin is polarized opposite to the applied magnetic field and the spins wind radially from the center towards the periphery. In Fig. 2, we depict the polarization along the field ($m_{z,\boldsymbol{r}}$) using a color scale and the in-plane polarization ($m_{x/y,\boldsymbol{r}}$) by arrows. More detailed radial and angular distributions of panel Fig. 2(e) are depicted in Fig. 3.

We estimate the size of an individual quantum skyrmion as the number of lattice sites over which the polarization changes its orientation once and the components orthogonal to the external field vanish. The radius can then be read out from Figs. 2 and 3 and results in $r_0 \approx 3a$ for $J = -0.5D$ and $K = 0$. These quantum skyrmion ground states occur not only for the fine-tuned parameters presented in Fig. 2, but in a wide range of intermediate values of the magnetic field. Furthermore, the emergence of individual skyrmions for small lattices is largely independent of the lattice geometry. While the effect of boundaries cannot be neglected for the small systems considered here, we verified that the size of an individual skyrmion is neither affected by the boundary conditions (see Fig. 2), nor the system diameter (see Fig. 6).

As we show in Fig. 2, for small magnetic fields the system state is a spin wave. This is characterized by a degenerate ground state, in which each possible ground state features an oscillation of the magnetization along a symmetry axis of the lattice. The large ground state degeneracy makes the spin wave phase notoriously difficult to simulate for tensor network states. In contrast, for large magnetic fields, the system reaches a ferromagnetic state, where all spins are polarized parallel to the external magnetic field. The bulk of the field-polarized ferromagnet is devoid of entanglement and can thus be most efficiently approximated by an MPS. For parameters which result in quantum skyrmion ground states, DMRG reliably converges within a few dozen sweeps and yields excellent MPS approximations with maximum truncation error $\Delta\rho \approx 10^{-6}$, even for small bond dimensions $M = 32$ [52]. For a detailed error discussion, we refer to our Methods section.

Entanglement. In order to probe whether the spins constituting a skyrmion are entangled, a genuine quantum feature of many-body systems, we compute the entanglement entropy of a suitable bipartition of the system. The latter is defined as $S = \mathrm{tr}(\rho_A \ln \rho_A)$, which can be understood as the von Neumann entropy of the reduced density matrix $\rho_A = \mathrm{tr}_B(\rho_{AB})$, obtained by splitting the set of lattice sites N into two disjoint sets A and B, and performing the partial trace over subsystem B. For our purposes, it is sufficient to fix A and B as two patches which are symmetric about the central site (see Section IV).

MPS are constructed to target states of small entropy by truncating the reduced density matrix to a dimension $\dim(\rho_A) \leq \chi$, which yields an upper bound for the entanglement entropy of an MPS state, $\tilde{S} = \ln \chi$, a quantity on the order of $1 - 10$ for typical simulations. The bulk of field-polarized states can be approximated by product states of spin-1/2 particles aligned to the axis of the magnetic field, and for those states one finds $S = 0$ up to small finite-size corrections. In contrast, for systems hosting a single quantum skyrmion, we obtain values for the entanglement entropy in the range $0.2 < S < 0.7$, which demonstrates the presence of significant entanglement in the spin-1/2 quantum skyrmion and indicating that they cannot be expressed as a product state. Finally, in the spin wave phase, we find the strongest entanglement where $0.7 < S$. Hence, using the entanglement entropy it is possible to define three disjoint intervals which allow us to differentiate between all phases encountered in the system, and we mark those intervals by hatched regions in Fig. 1.

The von Neumann entropy targets quantum correlations between bipartitions of the system, but does not provide local information about the entanglement between individual spin-1/2 pairs. To access the spatial distribution of entanglement, it is therefore more convenient to calculate the concurrence $C_{\boldsymbol{r}_1\boldsymbol{r}_2}$, defined for two lattice sites at positions $\boldsymbol{r}_1$ and $\boldsymbol{r}_2$. For a generic state it can be expressed through the root of the spectrum of the non-Hermitian matrix $R_{\boldsymbol{r}_1\boldsymbol{r}_2} = \rho_{\boldsymbol{r}_1\boldsymbol{r}_2}\tilde{\rho}_{\boldsymbol{r}_1\boldsymbol{r}_2}$, where $\rho_{\boldsymbol{r}_1\boldsymbol{r}_2} = \mathrm{tr}_{\boldsymbol{r}\notin\{\boldsymbol{r}_1,\boldsymbol{r}_2\}}(\rho)$ is the reduced density matrix of the two sites $\boldsymbol{r}_1$ and $\boldsymbol{r}_2$, and $\tilde{\rho}_{\boldsymbol{r}_1\boldsymbol{r}_2} = (\sigma_y \otimes \sigma_y)\rho^*_{\boldsymbol{r}_1\boldsymbol{r}_2}(\sigma_y \otimes \sigma_y)$ is a rotation of this reduced density matrix. The concurrence is then constructed from the square roots λ_i (ordered in decreasing order) of the eigenvalues of R,

$$C_{\boldsymbol{r}_1\boldsymbol{r}_2} = \max\{0, \lambda_1 - \lambda_2 - \lambda_3 - \lambda_4\}. \tag{4}$$

It is related to the entanglement of formation: for separable states C vanishes, and it increases monotonically towards the limit $C = 1$ for two maximally entangled spin-1/2's [53]. Using the concurrence, we obtain the space-resolved entanglement distribution between spin pairs in the different phases and present its quantitative distribution by green links in Fig. 1 (d-i).

For *spin wave states* (small magnetic field), we find a largely uniform entanglement distribution between nearest-neighbor spin pairs. Interestingly, for the spin wave states of larger lattices we find long-ranged concurrences between distant spin pairs (see Fig. 1(g)). We find concurrences below a maximum of $C \leq 0.16$ for the system depicted in Fig. 1(d). For the *field-polarized states* (large magnetic field), we find $C = 0$ in the bulk, indicating that the bulk spins are separable, and small nonzero values of $C \leq 0.065$ (maximum of Fig. 1(f)) only occur at the boundary due to the finite system size and strong DMI. Finally, for the *quantum skyrmion* (intermediate magnetic field), we find that the spins inside the

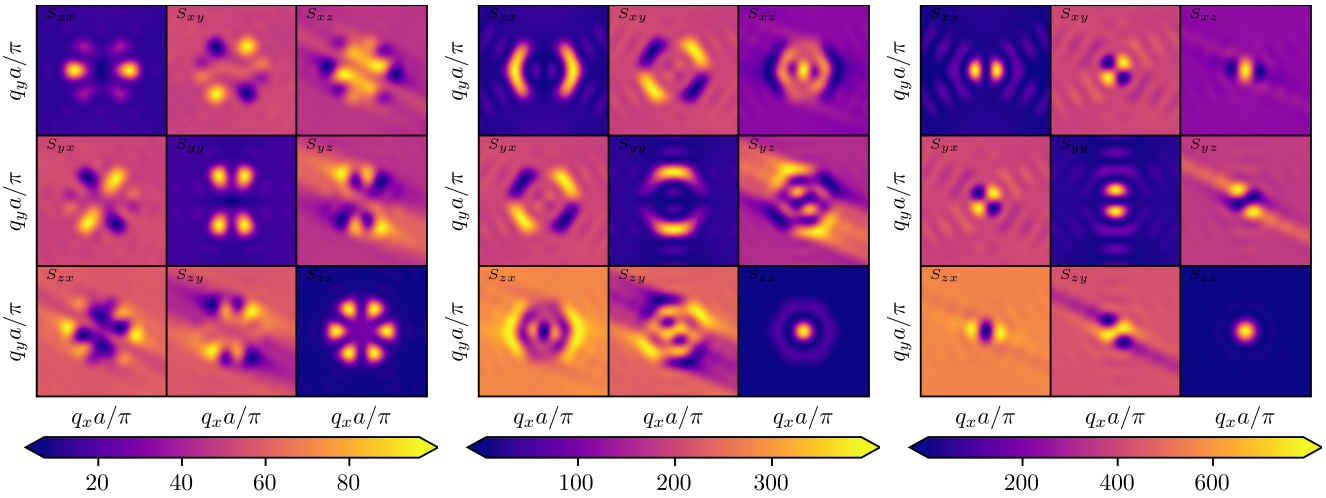

FIG. 4. Components of the structure factor $S_{\alpha\beta}(\boldsymbol{q})$ (in arbitrary units). Left: Spin wave state at $B = -0.1D$. Center: skyrmion state at $B = -0.5D$. Right: field-polarized state at $B = -1.0D$.

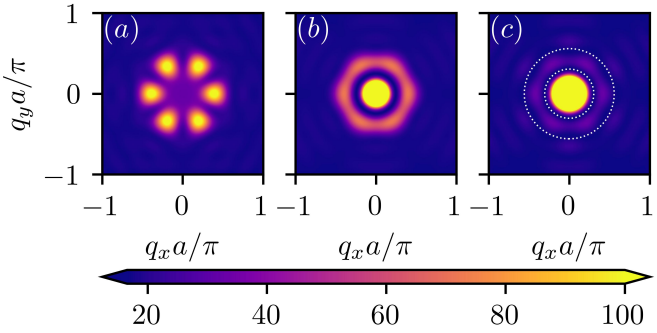

FIG. 5. Elastic magnetic differential scattering cross section $d\sigma/d\Omega$ (in arbitrary units). (a) Spin wave state at $B = -0.1D$, (b) skyrmion state at $B = -0.5D$, and (c) field-polarized state at $B = -1.0D$ for a triangular disk system of radius $R = 4a$. The geometry and local polarization is displayed in Fig. 2(d-f).

skyrmion quasiparticle are only weakly entangled, but we find concurrences $C \leq 0.13$ (maximum of Fig. 1(e)) at the outer rim spins of the skyrmion, signalling significant entanglement of the quantum skyrmion with the field-polarized environment (see Fig. 1(h)).

Structure factor and neutron scattering cross section. The Fourier components of the spin-spin correlation function are computed as:

$$S_{\alpha\beta}(\boldsymbol{q}) = \frac{1}{4}\sum_{\boldsymbol{r}\boldsymbol{r}'} \mathrm{e}^{\mathrm{i}\boldsymbol{q}\cdot(\boldsymbol{r}'-\boldsymbol{r})} \left\langle \hat{\sigma}_{\alpha,\boldsymbol{r}} \hat{\sigma}_{\beta,\boldsymbol{r}'} \right\rangle, \tag{5}$$

where $\alpha, \beta \in \{x, y, z\}$, $\boldsymbol{q} = (q_x, q_y, q_z)$ is the wave vector, and the expectation values of the Pauli operators $\hat{\sigma}_{\alpha,\boldsymbol{r}}$ are evaluated with the ground state obtained by the MPS simulations. From $S_{\alpha\beta}$, the elastic magnetic neutron scattering cross section $d\sigma/d\Omega$ at momentum transfer vector $\boldsymbol{q}$ is straightforwardly obtained as [54]:

$$\frac{d\sigma}{d\Omega}(\boldsymbol{q}) \propto \sum_{\alpha\beta} (\delta_{\alpha\beta} - \hat{q}_\alpha \hat{q}_\beta) S_{\alpha\beta}(\boldsymbol{q}), \tag{6}$$

where $\hat{\boldsymbol{q}} = \boldsymbol{q}/q = (\hat{q}_x, \hat{q}_y, \hat{q}_z)$. With respect to experiment we emphasize that $d\sigma/d\Omega$ corresponds to the scattering geometry which has the externally applied magnetic field $\boldsymbol{B} = B\hat{\boldsymbol{e}}_z$ parallel to the wave vector of the incoming neutron beam, and that the detector plane is spanned by the two components q_x and q_y of the scattering vector. In the limit of the small-angle approximation $q_z \approx 0$ can be neglected.

In Fig. 5 we display $d\sigma/d\Omega$ for the spin wave, skyrmion, and field-polarized states (see Fig. 4 for all components $S_{\alpha\beta}$ of the structure factor). Generally speaking, long-range magnetic ordering is signalled by the presence of Bragg peaks in $d\sigma/d\Omega$ at momentum transfers $\boldsymbol{q}$ corresponding to the wave vectors of the ordering. We expect additional diffuse magnetic scattering components in $d\sigma/d\Omega$ rooted in spatial variations of the spin orientation.

As expected, the cross section of the *field-polarized state* in Fig. 5(c) is isotropic and exhibits a single broad peak centered at $\boldsymbol{q} = 0$ mainly caused by the component S_{zz} parallel to the external field. The contributions in $S_{\alpha\beta}$ ($\alpha \in \{x, y\}$, $\beta \in \{x, y, z\}$) are attributed to finite-size effects, caused by a helical winding of $\langle \boldsymbol{S}_{\boldsymbol{r}} \rangle$ near the boundaries due to the strong DMI interaction (see Fig. 2). The azimuthal average of the cross section in Fig. 5(c), defined as $(2\pi)^{-1}\int_0^{2\pi} d\varphi (d\sigma/d\Omega)$ can be well described by the form factor of a uniformly polarized thin circular disc with a radius R corresponding to the cluster radius, i.e., $d\sigma/d\Omega(q) \propto [2J_1(qR)/(qR)]^2$, where $J_1(z)$ denotes the first-order Bessel function. To highlight this point, we display the first two minima of $[J_1(qR)/(qR)]^2$ (for $R = 4a$) by dotted white lines in Fig. 5(c) and find a very good agreement to the numerical data of the discrete

system. The *spin wave state* in Fig. 5(a) is a representative of a quantum helical phase, which is characterized by a superposition of spin spirals with wave vectors $\boldsymbol{q} \neq 0$, resulting in six pronounced Bragg peaks in $S_{zz}(\boldsymbol{q})$. We observe in the *skyrmion phase* a superposition of the two extreme limits: in particular, we find a Bragg peak at $\boldsymbol{q} = 0$, together with an off-diagonal Bragg "ring" caused by the radial polarization winding of the skyrmion (see Fig. 5(b)). The radius of this helical state can then be estimated as $r_0 = q_0^{-1} \approx 3a$ with $q_0 \approx 1/(3a)$ the momentum modulus of the $\boldsymbol{q} \neq 0$ Bragg ring, consistent with the estimate given in Fig. 3. Hence, the predicted quantum skyrmion profile yields a distinct signature in the measurable neutron scattering cross section and allows a determination of its size.

Quantum skyrmion lattice phase. After having discussed the properties of individual quantum skyrmions in the preceding paragraphs, we now turn to the phase diagram of the system. Our numerical technique makes it possible to reach system sizes much larger than that of individual skyrmions, which allows us to extrapolate towards a phase diagram in the thermodynamic limit. While the spin wave phase and the field-polarized phase remain unchanged when increasing the system size, at intermediate magnetic fields, the ground state for large lattices features a regular lattice of quantum skyrmions. Similar to their classical analogs, the individual skyrmions condense to a dense packing, and for larger system sizes we thus find quantum skyrmion chains and lattices, for which we plot examples in Fig. 6.

We elucidate the appearance and robustness of quantum skyrmion lattices as a function of external magnetic field, strength of DMI and perturbations of the form Eq. (2) due to uniaxial anisotropy. For this calculation, we have concentrated on a regular triangular lattice consisting of 81 sites ($L_1 = L_2 = 9$), for which we obtain a single centered skyrmion for $B = J = -0.5D$ in the unperturbed case $K = 0$ (see Fig. 2). We relax the fine-tuned parameter lines of Fig. 2 by variations of B and consider nonzero uniaxial anisotropy by increasing the absolute magnitude of K.

Based on our simulations, we predict the existence of three distinct quantum phases of our model: (i) a region hosting spin waves for weak field amplitudes, (ii) a valley for field strengths of the order of $B \approx -0.5D$, which features a quantum skyrmion lattice, and (iii) a field-polarized phase where spins align parallel to the external field. Spin wave states are characterized by a vanishing average polarization $\bar{m}^z$, whereas field-polarized states are maximally polarized (up to finite-size effects). As shown in Fig. 2, quantum skyrmions are located in a background of field-polarized spins, and as a consequence the state in the skyrmion lattice phase will have a finite polarization smaller than a corresponding field-polarized state. We numerically confirm this intuitive picture and find three disjoint intervals of average polarization $\bar{m}^z$ uniquely linked to each phase, which can be summarized in the zero temperature phase diagram presented in Fig. 1. Our results about the dependence of the skyrmion phase on the uniaxial anisotropy are in qualitative agreement with corresponding classical systems, where it is known that a weak uniaxial anisotropy has a tendency to stabilize skyrmion configurations at smaller magnetic fields [12, 55].

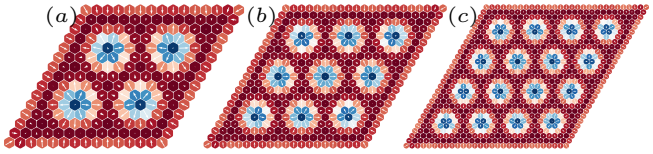

FIG. 6. Local polarization of regular rhomboid triangular lattice ground states at $J = B = -0.5D$ and $K = 0$. For parameters in the star-hatched region of Fig. 1(a) and larger systems, the quasiparticles are densely packed and form a skyrmion lattice.

We checked that the fine-tuned regime $J = -0.5D$ is not strictly necessary to enter the skyrmion lattice phase. By increasing the ferromagnetic exchange coupling to a value $J = -2D$, we obtain qualitatively similar results, which we present in Fig. 1(c) and in Fig. 1 panels (g)-(i). Similar values of the exchange coupling are encountered in recent thin film experiments [56]. Furthermore, we observe that the skyrmion radius increases with $-J/D$ (compare Fig. 1(e) and (h)), such that quite large spin-1/2 systems might be needed to resolve even individual quantum skyrmions. Based on our results for $J = -0.5D$ we conjecture that the skyrmion lattice phase should also exist for such cases where the individual quasiparticles have a larger radius, but due to limitations dictated by the numerical complexity (which we discuss in Section IV), other numerical techniques must be consulted to make quantitative predictions about the phase diagram for $-J/D \gg 0.5$.

III. DISCUSSION

We have demonstrated that the ground state of the two-dimensional ferromagnetic spin-1/2 Heisenberg model in the presence of DMI hosts quantum skyrmions at intermediate magnetic fields $B \approx J = -D/2$. The resulting magnetic textures are characterized by a central spin pointing opposite to the direction of the applied magnetic field and winds radially outwards towards the field-polarized environment, similar to a classical Néel skyrmion. The existence of quantum skyrmions yields experimental signatures in the position-dependent magnetization, the average polarization and in the structure factor, and we showed that these observables allow a distinction between a spin wave phase at small magnetic fields, a skyrmion phase at intermediate magnetic fields, and a field-polarized phase at large magnetic fields.

While the spin texture is reminiscent of classical skyrmions, we should point out that in the present case

the skyrmion phase arises as a quantum ground state at zero temperature. In contrast, classical skyrmions typically occur at finite temperatures and result from a minimization of the free energy. Moreover, our examination of the resulting quantum state using the entanglement entropy and the concurrence has revealed that the quantum skyrmion state features significant entanglement shared between spin pairs of the skyrmion boundary. This shows that a semiclassical treatment of the quantum skyrmion based on a classical magnetic texture would not necessarily capture the internal degrees of freedom of a quantum skyrmion.

Towards larger system sizes, we found that the quantum skyrmion phase is actually characterized by a regular lattice of skyrmions. As the size of an individual skyrmions is determined by the system parameters B, J, D, and K, a regular lattice requires commensurability between the lattice size and the skyrmion size. While our numerical simulations cannot reach the limit of infinite system size, our results allow us to extrapolate that the ground state in the thermodynamic limit features a dense packing of quantum skyrmion textures. Each of these quantum skyrmions has entanglement localized near its domain wall, but the entanglement between different skyrmions is small, which suggests that they can be approximated as individual quasiparticles.

We expect that our results may guide the development of an effective analytical field theory of the quantum skyrmion phase. Based on our experience, we conclude that variational tensor networks provide a suitable numerical technique to study these systems. This is not surprising for gapped quantum phases with short-range interactions and bounded entanglement. Nevertheless, using MPS for a two-dimensional system is not without pitfalls, as the necessary mapping on a one-dimensional system causes non-local interactions. We have made sure that our results have fully converged for lattice sizes corresponding to individual skyrmions. However, we have seen that the numerical errors grows larger for the system sizes required for 4×4 skyrmion lattices (29×29 spin-1/2 in total). For such large systems, we expect our results to be only qualitatively correct.

Regarding alternative numerical schemes, we have verified that our MPS results agree quantitatively with all available results from exact diagonalization. We have also compared our results to variational methods based on neural-network quantum states. However, we found significant deviations between the exact result and neural-network states even for small system sizes, and the error was already on the order of 10% for the energy eigenvalues. This suggests that neural-network states do not provide an efficient variational ansatz for mesoscopic spin systems with DMI. We expect that quantum Monte-Carlo simulations might be useful to go to larger system sizes. However, the inclusion of DMI typically brings about a sign problem which hinders convergence. Other promising tensor network states for 2D spin systems with DMI are variational tree tensor network states [57] and projected entangled pair states (PEPS) [58]. We expect finite PEPS to outperform MPS for larger spin-1/2 systems hosting skyrmion lattices, especially since recently a more efficient gradient-based optimization has been developed, based on automatic differentiation techniques [51, 59, 60].

IV. METHODS

Matrix Product States. Tensor networks provide an important numerical toolbox in computational physics and have been applied successfully to countless interacting and strongly correlated systems [61–64]. One of the most established algorithms, called density matrix renormalization group (DMRG) [65], is understood as a sequential variational optimization of two adjacent MPS tensors until convergence is reached. Let M be the bond dimension (the maximum dimension of the contracted links in the MPS decomposition), N the number of physical sites and M_H the dimension of the Hamiltonian matrix product operator, then the traditional DMRG reformulated in terms of MPS bears a numerical complexity of $\mathcal{O}(NM^3M_H^2)$ [66]. The bond dimension is directly related to the so-called Schmidt decomposition $|\psi\rangle = \sum_{i=1}^{M} s_i |\psi_{A,i}\rangle |\psi_{B,i}\rangle$ in which A and B form an arbitrary bipartition of the lattice and $|\psi_{\alpha,i}\rangle \in \mathcal{H}_\alpha$ forms a complete basis in the Hilbert space of the part $\alpha \in \{A, B\}$. M is therefore in general an extensive quantity in the number of sites and diverges in the thermodynamic limit. If the target state of a one-dimensional system obeys an area law of the quantum entanglement, the von Neumann entropy is guaranteed to be a finite constant [67]. As a consequence M remains finite in the thermodynamic limit and MPS becomes exact, which explains the success of DMRG applied to one-dimensional quantum systems. Despite its limitations in two dimensions, DMRG is frequently applied to ladder systems and can even yield reliable results for strongly correlated lattices, especially in case of quantum spin-1/2 Heisenberg models.

We typically start with random MPS initial states of bond dimensions up to $M \leq 1024$, followed by sequential variational optimizations ("sweeping") of two adjacent tensors (two-site DMRG). The two-site DMRG allows to estimate the truncation error $\Delta\rho = \sum_{i=M+1}^{\infty} s_i^2$, which we use in Fig. 7 to extrapolate towards results without numerical errors. To ensure that we display converged results only, we carefully monitor local spin expectation values and stop the simulation if changes in the observables become smaller than $\delta = 10^{-10}$. Since we use DMRG in two spatial dimensions, convergence to a spin wave state may require many sweeps, on the order of $100 - 1000$. The quality of the approximate ground state with energy $E(M) = \langle\psi(M)|\hat{H}|\psi(M)\rangle$ can be estimated

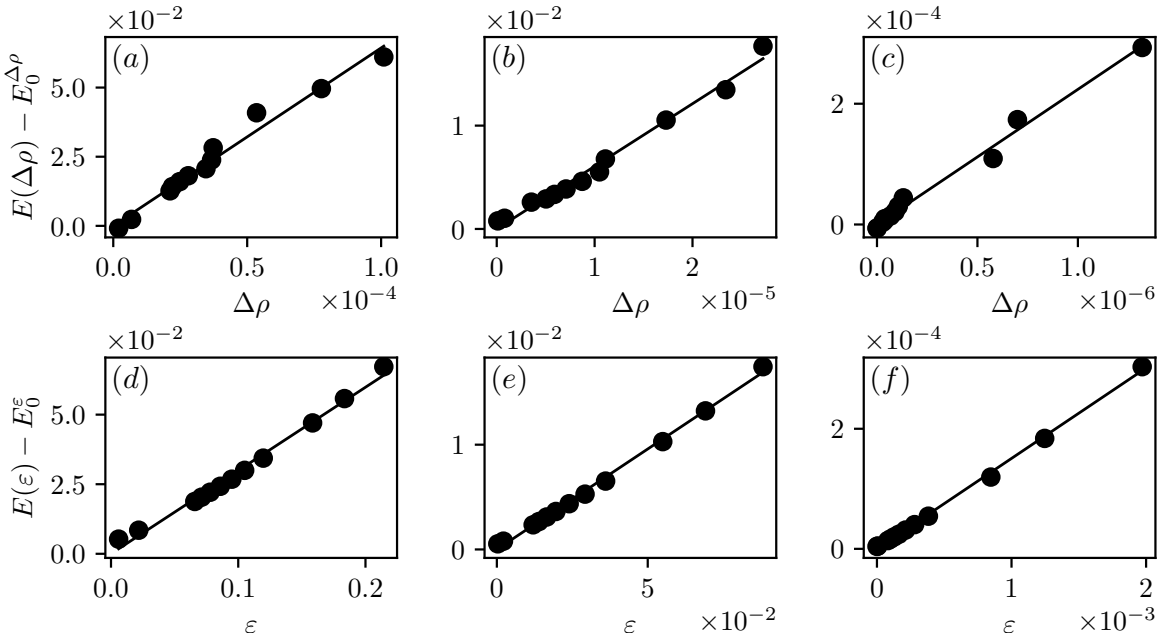

FIG. 7. Energy extrapolations for the three systems plotted in Fig. 2(d)-(f). Energy and error of the spin wave states are displayed in panels (a) and (d), of skyrmion states in panels (b) and (e) and of field-polarized states in panels (c) and (f). The black line corresponds to a least squares fit, whose energy offset E_0 and error is displayed in Table I.

by the energy variance

$$\varepsilon(M) = \left\langle \psi(M) \middle| \left(\hat{H} - E(M)\right)^2 \middle| \psi(M) \right\rangle . \qquad (7)$$

By construction, $\varepsilon = 0$ for exact eigenstates of the Hamiltonian. Since MPS approximates the wave function with a finite bond dimension M, we have $\varepsilon(M) > 0$ and $\lim_{M\to\infty} \varepsilon(M) = 0$ in general. Similarly, $\lim_{M\to\infty} E(M) = E_0$ converges to the true eigenstate energy. In order to estimate the numerical error of our approximate wave functions, we perform linear extrapolations of the energy scaled against the truncation error [22] and the energy variance [37]. The outcomes of this extrapolation is presented in Fig. 7 and Table I. We

B/D	-0.1	-0.5	-1.0
$E_0^{\Delta\rho}$	$-34.85093(9)$	$-41.024253(4)$	$-53.428962927(1)$
E_0^{ε}	$-34.85707(4)$	$-41.024009(1)$	$-53.4289732208(1)$

TABLE I. Least squares energy fit for the data of Fig. 7.

want to stress that the MPS approximations corresponding to skyrmion and field-polarized states easily reach convergence within a few dozen sweeps and follow the expected linear trend in the approximation errors $\Delta\rho$ and ε [52].

Changes of the local spin expectation values beyond $M = 128$ are invisible to the naked eye when displayed on the scales used in the main text such that a detailed error extrapolation thereof is not needed. A word of caution in case of spin wave states: As we already explained in the main text, these states are difficult to simulate using MPS due to the large degeneracy of the ground state manifold. This leads to some issues in reaching convergence (up to 1000 sweeps are needed) which for too small bond dimensions may even cause DMRG to get stuck in local energy minima corresponding to excited eigenstates. In the spin wave phase and for large lattices, MPS is thus not always reliably converging to approximations of the global ground state, but converges under some circumstances to low-lying excited states with less entanglement – with outcomes roughly comparable with those presented in Ref. [26].

Mapping from 2D to 1D. Before we can apply DMRG to the system at hand, the 2D lattice must be mapped to a 1D chain. This is performed by a sequential numbering of the lattice nodes with major ordering along an arbitrary axis (zigzag ordering). We choose the major axis to be $\hat{\boldsymbol{a}}_2$. The map from 2D lattice nodes to 1D chains then reads $f(\boldsymbol{r}) = f(n_1, n_2) = \sum_{i_2<n_2} L_2(i_2) + n_2$, where $L_2(n)$ encodes the lattice open boundary conditions along $\hat{\boldsymbol{a}}_2$ and $\boldsymbol{r} = \boldsymbol{r}(n_1, n_2) = \sum_i n_i \hat{\boldsymbol{a}}_i$. As a result, the lattice Hamiltonian $\hat{H} = \sum_{\langle \boldsymbol{r},\boldsymbol{r}'\rangle} \hat{H}_{\boldsymbol{r},\boldsymbol{r}'} + \sum_{\boldsymbol{r}} \hat{H}_{\boldsymbol{r}}$ is mapped to a chain Hamiltonian $\hat{H} = \sum_{\langle \boldsymbol{r},\boldsymbol{r}'\rangle} \hat{H}_{f(\boldsymbol{r}),f(\boldsymbol{r}')} + \sum_{\boldsymbol{r}} \hat{H}_{f(\boldsymbol{r})}$. To simplify the remaining discussion, we now assume square or rhomboid boundary conditions (panels (a-c) or (m-o) of Fig. 2), such that $L_2(n) = L_2$. On-site contributions remain local, nearest neighbor interactions along the major axis remain short ranged, but the interactions along $\hat{\boldsymbol{a}}_1$ are attributed an extended range

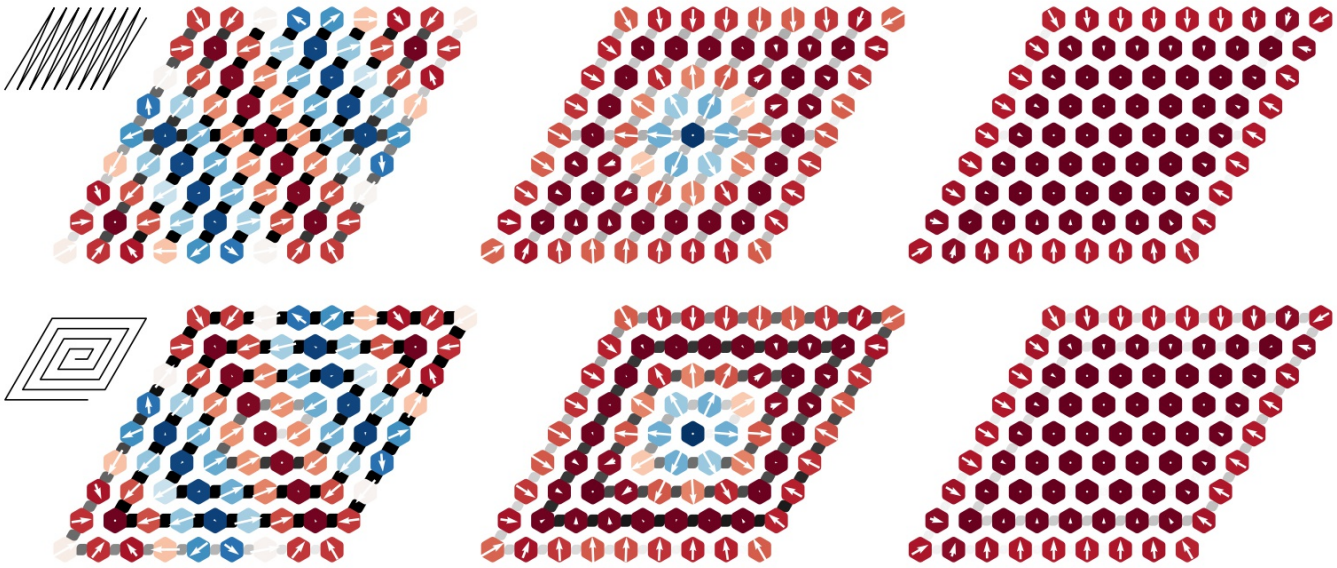

FIG. 8. The three distinct ground states of Eq. (1) (spin wave, skyrmion, field-polarized) obtained by two different 2D→1D mapping strategies: zigzag (top row) vs spiral (bottom row). The polarization is depicted by colors and arrows, and the von Neumann entropy encoded by links in grayscale. Whereas the von Neumann entropy is rather small and homogeneously distributed for the zigzag order, it appears not only larger but also inhomogeneous for the spiral ordered 1D chain.

$|f(\boldsymbol{r}) - f(\boldsymbol{r} \pm \hat{\boldsymbol{a}}_1)| = L_2$. This results in a growth of the dimension of the Hamiltonian matrix product operator $M_H \propto L_2$, and the total numerical cost of the DMRG scales as $\sim L_1(L_2 M)^3$. Note that the choice of our mapping preserves locality of the interaction along one direction. In an attempt to remove this bias, we checked the resulting MPS quality for a different mapping, starting at the central spin-1/2 site and ordered radially outward (spiral ordering). Using the spiral ordering, we can confirm using the von Neumann entropy that the outer rim of the skyrmion is strongly entangled with its environment, a conclusion we had also reached based on the concurrence. Compared to the other proposition, the spiral mapping results in a higher variational energy, likely the result of the inhomogeneous entanglement distribution (see Fig. 8). Since entanglement can be created by nonlocal transformations, it is known that certain mappings are beneficial compared to others, which can be utilized to obtain a substantial improvement of the overall simulation quality [68]. For the results presented in the main text, we consistently use the zigzag order. Our DMRG code is based on the Julia package iTensors [69], and we published a condensed version (missing some technical details discussed in this section) on GitHub [52].

[1] A. Bogdanov and D. Yablonskii, Thermodynamically stable "vortices" in magnetically ordered crystals. The mixed state of magnets, Zh. Eksp. Teor. Fiz **95**, 182 (1989).

[2] A. Bogdanov and A. Hubert, Thermodynamically stable magnetic vortex states in magnetic crystals, Journal of Magnetism and Magnetic Materials **138**, 255 (1994).

[3] U. K. Rößler, A. N. Bogdanov, and C. Pfleiderer, Spontaneous Skyrmion Ground States in Magnetic Metals, Nature **442**, 797 (2006).

[4] A. Neubauer, C. Pfleiderer, B. Binz, A. Rosch, R. Ritz, P. G. Niklowitz, and P. Böni, Topological Hall Effect in the *A* Phase of MnSi, Phys. Rev. Lett. **102**, 186602 (2009).

[5] S. Mühlbauer, B. Binz, F. Jonietz, C. Pfleiderer, A. Rosch, A. Neubauer, R. Georgii, and P. Böni, Skyrmion Lattice in a Chiral Magnet, Science **323**, 915 (2009).

[6] X. Z. Yu, Y. Onose, N. Kanazawa, J. H. Park, J. H. Han, Y. Matsui, N. Nagaosa, and Y. Tokura, Real-space observation of a two-dimensional skyrmion crystal, Nature **465**, 901 (2010).

[7] F. Jonietz, S. Mühlbauer, C. Pfleiderer, A. Neubauer, W. Münzer, A. Bauer, T. Adams, R. Georgii, P. Böni, R. A. Duine, K. Everschor, M. Garst, and A. Rosch, Spin Transfer Torques in MnSi at Ultralow Current Densities, Science **330**, 1648 (2010).

[8] A. Fert, V. Cros, and J. Sampaio, Skyrmions on the track, Nature Nanotechnology **8**, 152 (2013).

[9] R. Wiesendanger, Nanoscale Magnetic Skyrmions in Metallic Films and Multilayers: A New Twist for Spintronics, Nature Reviews Materials **1**, 1 (2016).

[10] K. Everschor-Sitte, J. Masell, R. M. Reeve, and M. Kläui, Perspective: Magnetic skyrmions — Overview of recent progress in an active research field, Journal of Applied Physics **124**, 240901 (2018).

[11] A.-O. Mandru, O. Yıldırım, R. Tomasello, P. Heistracher, M. Penedo, A. Giordano, D. Suess, G. Finocchio, and H. J. Hug, Coexistence of distinct skyrmion phases observed in hybrid ferromagnetic/ferrimagnetic multilayers, Nature Communications **11**, 10.1038/s41467-020-20025-2 (2020).

[12] S. Heinze, K. von Bergmann, M. Menzel, J. Brede, A. Kubetzka, R. Wiesendanger, G. Bihlmayer, and S. Blügel, Spontaneous Atomic-Scale Magnetic Skyrmion Lattice in Two Dimensions, Nature Physics **7**, 713 (2011).

[13] H. Ochoa and Y. Tserkovnyak, Quantum Skyrmionics, Int. J. Mod. Phys. B **33**, 1930005 (2019).

[14] C. Psaroudaki, S. Hoffman, J. Klinovaja, and D. Loss, Quantum Dynamics of Skyrmions in Chiral Magnets, Phys. Rev. X **7**, 041045 (2017).

[15] R. Takashima, H. Ishizuka, and L. Balents, Quantum Skyrmions in Two-Dimensional Chiral Magnets, Phys. Rev. B **94**, 134415 (2016).

[16] O. Janson, I. Rousochatzakis, A. A. Tsirlin, M. Belesi, A. A. Leonov, U. K. Rößler, J. van den Brink, and H. Rosner, The quantum nature of skyrmions and half-skyrmions in Cu2OSeO3, Nature Communications **5**, 10.1038/ncomms6376 (2014).

[17] S. Seki, X. Z. Yu, S. Ishiwata, and Y. Tokura, Observation of Skyrmions in a Multiferroic Material, Science **336**, 198 (2012), https://science.sciencemag.org/content/336/6078/198.full.pdf.

[18] V. Lohani, C. Hickey, J. Masell, and A. Rosch, Quantum Skyrmions in Frustrated Ferromagnets, Phys. Rev. X **9**, 041063 (2019).

[19] O. M. Sotnikov, V. V. Mazurenko, J. Colbois, F. Mila, M. I. Katsnelson, and E. A. Stepanov, Probing the topology of the quantum analog of a classical skyrmion, Phys. Rev. B **103**, L060404 (2021).

[20] P. Siegl, E. Y. Vedmedenko, M. Stier, M. Thorwart, and T. Posske, Controlled Creation of Quantum Skyrmions, arXiv:2110.00348 [cond-mat, physics:quant-ph] (2021), arXiv:2110.00348 [cond-mat, physics:quant-ph].

[21] L. Capriotti, D. J. Scalapino, and S. R. White, Spin-liquid versus dimerized ground states in a frustrated heisenberg antiferromagnet, Physical Review Letters **93**, 10.1103/physrevlett.93.177004 (2004).

[22] S. R. White and A. L. Chernyshev, Neél order in square and triangular lattice heisenberg models, Phys. Rev. Lett. **99**, 127004 (2007).

[23] A. B. Kallin, I. González, M. B. Hastings, and R. G. Melko, Valence bond and von neumann entanglement entropy in heisenberg ladders, Physical Review Letters **103**, 10.1103/physrevlett.103.117203 (2009).

[24] S. Yan, D. A. Huse, and S. R. White, Spin-liquid ground state of the s=1/2 kagome heisenberg antiferromagnet, Science **332**, 1173 (2011).

[25] S. Depenbrock, I. P. McCulloch, and U. Schollwöck, Nature of the spin-liquid ground state of the $s = 1/2$ heisenberg model on the kagome lattice, Phys. Rev. Lett. **109**, 067201 (2012).

[26] H.-C. Jiang, Z. Wang, and L. Balents, Identifying topological order by entanglement entropy, Nature Physics **8**, 902 (2012).

[27] S. Nishimoto, N. Shibata, and C. Hotta, Controlling frustrated liquids and solids with an applied field in a kagome heisenberg antiferromagnet, Nature Communications **4**, 10.1038/ncomms3287 (2013).

[28] Z. Zhu, D. A. Huse, and S. R. White, Weak plaquette valence bond order in the $s = 1/2$ honeycomb j_1-j_2 heisenberg model, Physical Review Letters **110**, 10.1103/physrevlett.110.127205 (2013).

[29] S.-S. Gong, W. Zhu, D. N. Sheng, O. I. Motrunich, and M. P. A. Fisher, Plaquette ordered phase and quantum phase diagram in the spin-1/2 j_1-j_2 square heisenberg model, Physical Review Letters **113**, 10.1103/physrevlett.113.027201 (2014).

[30] Y.-C. He, D. N. Sheng, and Y. Chen, Chiral spin liquid in a frustrated anisotropic kagome heisenberg model, Physical Review Letters **112**, 10.1103/physrevlett.112.137202 (2014).

[31] F. B. Ramos and J. C. Xavier, N-leg spin-s heisenberg ladders: A density-matrix renormalization group study, Physical Review B **89**, 10.1103/physrevb.89.094424 (2014).

[32] F. Kolley, S. Depenbrock, I. P. McCulloch, U. Schollwöck, and V. Alba, Phase diagram of the j_1-j_2 heisenberg model on the kagome lattice, Physical Review B **91**, 10.1103/physrevb.91.104418 (2015).

[33] K. Shinjo, S. Sota, and T. Tohyama, Density-matrix renormalization group study of the extended kitaev-heisenberg model, Physical Review B **91**, 10.1103/physrevb.91.054401 (2015).

[34] W.-J. Hu, S.-S. Gong, W. Zhu, and D. N. Sheng, Competing spin-liquid states in the spin-1/2 heisenberg model on the triangular lattice, Physical Review B **92**, 10.1103/physrevb.92.140403 (2015).

[35] Y. Iqbal, W.-J. Hu, R. Thomale, D. Poilblanc, and F. Becca, Spin liquid nature in the heisenberg j_1-j_2 triangular antiferromagnet, Physical Review B **93**, 10.1103/physrevb.93.144411 (2016).

[36] K. Morita and N. Shibata, Multiple magnetization plateaus and magnetic structures in the s=1/2 heisenberg model on the checkerboard lattice, Physical Review B **94**, 10.1103/physrevb.94.140404 (2016).

[37] S. N. Saadatmand and I. P. McCulloch, Symmetry fractionalization in the topological phase of the spin-1/2 j_1-j_2 triangular heisenberg model, Physical Review B **94**, 10.1103/physrevb.94.121111 (2016).

[38] Y.-C. He, M. P. Zaletel, M. Oshikawa, and F. Pollmann, Signatures of dirac cones in a dmrg study of the kagome heisenberg model, Physical Review X **7**, 10.1103/physrevx.7.031020 (2017).

[39] S. Capponi, Numerical study of magnetization plateaus in the spin-1/2 heisenberg antiferromagnet on the checkerboard lattice, Physical Review B **95**, 10.1103/physrevb.95.014420 (2017).

[40] S. N. Saadatmand and I. P. McCulloch, Detection and characterization of symmetry-broken long-range orders in the spin-1/2 triangular heisenberg model, Physical Review B **96**, 10.1103/physrevb.96.075117 (2017).

[41] M. Gohlke, R. Verresen, R. Moessner, and F. Pollmann, Dynamics of the kitaev-heisenberg model, Physical Review Letters **119**, 10.1103/physrevlett.119.157203 (2017).

[42] L. Wang and A. W. Sandvik, Critical level crossings and gapless spin liquid in the square-lattice spin-1/2 j_1-j_2 heisenberg antiferromagnet, Physical Review Letters **121**, 10.1103/physrevlett.121.107202 (2018).

[43] J.-Y. Chen, L. Vanderstraeten, S. Capponi, and D. Poilblanc, Non-abelian chiral spin liquid in a quantum antiferromagnet revealed by an ipeps study, Physical Review B **98**, 10.1103/physrevb.98.184409 (2018).

[44] R. Verresen, F. Pollmann, and R. Moessner, Quantum dynamics of the square-lattice heisenberg model, Physical Review B **98**, 10.1103/physrevb.98.155102 (2018).

[45] R. Haghshenas, W.-W. Lan, S.-S. Gong, and D. N. Sheng, Quantum phase diagram of spin-1 J_1-J_2 heisenberg model on the square lattice: An infinite projected entangled-pair state and density matrix renormalization group study, Phys. Rev. B **97**, 184436 (2018).

[46] S.-S. Gong, W. Zheng, M. Lee, Y.-M. Lu, and D. N. Sheng, Chiral spin liquid with spinon fermi surfaces in the spin-1/2 triangular heisenberg model, Physical Review B **100**, 10.1103/physrevb.100.241111 (2019).

[47] S. Hu, W. Zhu, S. Eggert, and Y.-C. He, Dirac spin liquid on the spin-1/2 triangular heisenberg antiferromagnet, Physical Review Letters **123**, 10.1103/physrevlett.123.207203 (2019).

[48] X.-Y. Dong and D. N. Sheng, Spin-1 kitaev-heisenberg model on a honeycomb lattice, Physical Review B **102**, 10.1103/physrevb.102.121102 (2020).

[49] R. Schäfer, I. Hagymási, R. Moessner, and D. J. Luitz, Pyrochlore s=1/2 heisenberg antiferromagnet at finite temperature, Physical Review B **102**, 10.1103/physrevb.102.054408 (2020).

[50] I. Hagymási, R. Schäfer, R. Moessner, and D. J. Luitz, Possible inversion symmetry breaking in the s=1/2 pyrochlore heisenberg magnet, Physical Review Letters **126**, 10.1103/physrevlett.126.117204 (2021).

[51] W.-Y. Liu, S.-S. Gong, Y.-B. Li, D. Poilblanc, W.-Q. Chen, and Z.-C. Gu, Gapless quantum spin liquid and global phase diagram of the spin-1/2 j_1-j_2 square antiferromagnetic heisenberg model (2021), arXiv:2009.01821 [cond-mat.str-el].

[52] A. Haller, Skyrmion MPS, `https://github.com/hallerinos/skyrmion_mps` (2021).

[53] W. K. Wootters, Entanglement of Formation of an Arbitrary State of Two Qubits, Phys. Rev. Lett. **80**, 2245 (1998).

[54] S. W. Lovesey, *Theory of Neutron Scattering from Condensed Matter*, Vol. I and II (Clarendon Press, Oxford, 1984).

[55] N. Romming, C. Hanneken, M. Menzel, J. E. Bickel, B. Wolter, K. von Bergmann, A. Kubetzka, and R. Wiesendanger, Writing and Deleting Single Magnetic Skyrmions, Science **341**, 636 (2013).

[56] E. Y. Vedmedenko, P. Riego, J. A. Arregi, and A. Berger, Interlayer Dzyaloshinskii-Moriya Interactions, Phys. Rev. Lett. **122**, 257202 (2019).

[57] Y.-Y. Shi, L.-M. Duan, and G. Vidal, Classical simulation of quantum many-body systems with a tree tensor network, Phys. Rev. A **74**, 022320 (2006).

[58] F. Verstraete, V. Murg, and J. Cirac, Matrix product states, projected entangled pair states, and variational renormalization group methods for quantum spin systems, Advances in Physics **57**, 143 (2008).

[59] H.-J. Liao, J.-G. Liu, L. Wang, and T. Xiang, Differentiable programming tensor networks, Phys. Rev. X **9**, 031041 (2019).

[60] J. Hasik, D. Poilblanc, and F. Becca, Investigation of the néel phase of the frustrated heisenberg antiferromagnet by differentiable symmetric tensor networks, SciPost Physics **10**, 10.21468/scipostphys.10.1.012 (2021).

[61] I. Cirac, D. Perez-Garcia, N. Schuch, and F. Verstraete, Matrix product states and projected entangled pair states: Concepts, symmetries, and theorems, arXiv preprint arXiv:2011.12127 (2020).

[62] M. C. Bañuls, R. Blatt, J. Catani, A. Celi, J. I. Cirac, M. Dalmonte, L. Fallani, K. Jansen, M. Lewenstein, S. Montangero, C. A. Muschik, B. Reznik, E. Rico, L. Tagliacozzo, K. V. Acoleyen, F. Verstraete, U.-J. Wiese, M. Wingate, J. Zakrzewski, and P. Zoller, Simulating lattice gauge theories within quantum technologies, The European Physical Journal D **74**, 10.1140/epjd/e2020-100571-8 (2020).

[63] A. Baiardi and M. Reiher, The density matrix renormalization group in chemistry and molecular physics: Recent developments and new challenges, The Journal of Chemical Physics **152**, 040903 (2020).

[64] S. Paeckel, T. Köhler, A. Swoboda, S. R. Manmana, U. Schollwöck, and C. Hubig, Time-evolution methods for matrix-product states, Annals of Physics **411**, 167998 (2019).

[65] S. R. White, Density matrix formulation for quantum renormalization groups, Phys. Rev. Lett. **69**, 2863 (1992).

[66] U. Schollwöck, The Density Matrix Renormalization Group in the Age of Matrix Product States, Ann. Phys. January 2011 Special Issue, **326**, 96 (2011).

[67] M. B. Hastings, An area law for one-dimensional quantum systems, Journal of Statistical Mechanics: Theory and Experiment **2007**, P08024 (2007).

[68] G. Cataldi, A. Abedi, G. Magnifico, S. Notarnicola, N. D. Pozza, V. Giovannetti, and S. Montangero, Hilbert curve vs Hilbert space: exploiting fractal 2D covering to increase tensor network efficiency, Quantum **5**, 556 (2021).

[69] M. Fishman, S. R. White, and E. M. Stoudenmire, The ITensor software library for tensor network calculations (2020), arXiv:2007.14822.

[70] F. Vicentini, D. Hofmann, A. Szabó, D. Wu, C. Roth, C. Giuliani, G. Pescia, J. Nys, V. Vargas-Calderon, N. Astrakhantsev, and G. Carleo, NetKet 3: Machine Learning Toolbox for Many-Body Quantum Systems (2021), arXiv:2112.10526 [quant-ph].

Acknowledgements The authors acknowledge financial support from the National Research Fund of Luxembourg (FNR) under the following grants: ATTRACT A14/MS/7556175/MoMeSys, CORE C20/MS/14764976/TopRel, and CORE SANS4NCC. This research was supported in part by the National Science Foundation under Grant No. NSF PHY-1748958.

Author contributions T. L. Schmidt, A. Michels and S. Groenendijk developed the project idea. The ED and MPS calculations were carried out by A. Haller. NetKet [70] simulations were performed by A. Habibi. The manuscript and the supplement were written by A. Haller, A. Michels and T. L. Schmidt. All the authors contributed to the analysis and interpretation of the results.